PNAS RESEARCH ARTICLE | BIOPHYSICS AND COMPUTATIONAL BIOLOGY OPEN ACCESS

Definition of a saxitoxin (STX) binding code enables discovery and characterization of the anuran saxiphilin family

Zhou Chen[a,1], Sandra Zakrzewska[a,1], Holly S. Hajare[b], Aurora Alvarez-Buylla[c], Fayal Abderemane-Ali[a], Maximiliana Bogan[c], Dave Ramirez[c], Lauren A. O'Connell[c], J. Du Bois[b], and Daniel L. Minor, Jr.[a,d,e,f,g,h,2]

Edited by Nieng Yan, Princeton University, Princeton, NJ; received June 12, 2022; accepted September 19, 2022

American bullfrog (*Rana castesbeiana*) saxiphilin (*Rc*Sxph) is a high-affinity "toxin sponge" protein thought to prevent intoxication by saxitoxin (STX), a lethal bis-guanidinium neurotoxin that causes paralytic shellfish poisoning (PSP) by blocking voltage-gated sodium channels (Na_Vs). How specific *Rc*Sxph interactions contribute to STX binding has not been defined and whether other organisms have similar proteins is unclear. Here, we use mutagenesis, ligand binding, and structural studies to define the energetic basis of Sxph:STX recognition. The resultant STX "recognition code" enabled engineering of *Rc*Sxph to improve its ability to rescue Na_Vs from STX and facilitated discovery of 10 new frog and toad Sxphs. Definition of the STX binding code and Sxph family expansion among diverse anurans separated by ∼140 My of evolution provides a molecular basis for understanding the roles of toxin sponge proteins in toxin resistance and for developing novel proteins to sense or neutralize STX and related PSP toxins.

saxitoxin | saxiphilin | toxin resistance | anuran

Significance

Saxitoxin (STX) is a lethal neurotoxin made by cyanobacteria and dinoflagellates associated with oceanic red tides. Its accumulation in seafood causes paralytic shellfish poisoning (PSP), a public health hazard that is increasing due to climate change. Bullfrog saxiphilin (*Rc*Sxph) is a soluble STX binding protein that acts as a 'toxin sponge' involved in toxin resistance. Studying *Rc*Sxph:STX interaction energetics defines a STX 'recognition code' that enabled discovery of ten Sxphs in frogs and toads separated by ∼140 million years of evolution. These findings provide a molecular basis for understanding the roles of toxin sponge proteins in toxin resistance and should enable STX binding site identification in natural proteins and design of proteins to sense or neutralize STX and related toxins.

Saxitoxin (STX), one of the most potent nonpeptidyl neurotoxins, blocks the bioelectrical signals in nerve and muscle required for life by inhibiting select voltage-gated sodium channel (Na_V) isoforms (1–3). Cyanobacteria and dinoflagellate species associated with oceanic red tides produce this bis-guanidinium small molecule and its congeners, whose accumulation in seafood can cause paralytic shellfish poisoning (PSP), a commercial fishing and public health hazard of growing importance due to climate change (1, 3–5). Its lethality has also earned STX the unusual distinction of being the only marine toxin declared a chemical weapon (1, 3). Select vertebrates, particularly frogs, resist STX poisoning (6–9), a property that is thought to rely on the ability of the soluble "toxin sponge" protein saxiphilin (Sxph) to sequester STX (8, 9). Recent structural studies (10) defined the molecular architecture of the American bullfrog [*Rana* (*Lithobates*) *castesbeiana*] Sxph (*Rc*Sxph) (8, 11–14) showing that this 91-kDa soluble, transferrin-related protein from frog heart and plasma has a single, high-affinity STX binding site on its C lobe. Remarkably, even though *Rc*Sxph and Na_Vs are unrelated, both engage STX through similar types of interactions (10). This structural convergence raises the possibility that determination of the factors that underlie the high-affinity Sxph:STX interaction could provide a generalizable molecular recognition code for STX that would enable the identification or engineering of STX binding sites in natural and designed proteins.

To characterize *Rc*Sxph:STX interactions in detail, we developed a suite of assays comprising thermofluor (TF) measurements of ligand-induced changes in *Rc*Sxph stability, fluorescence polarization (FP) binding to a fluorescein-labeled STX, and isothermal titration calorimetry (ITC). We paired these assays with a scanning mutagenesis strategy (15, 16) to dissect the energetic contributions of *Rc*Sxph STX binding pocket residues. These studies show that the core *Rc*Sxph STX recognition code comprises two "hot spot" triads. One engages the STX tricyclic bis-guanidinium core through a pair of carboxylate groups and a cation–π interaction (17) in a manner that underscores the convergent STX recognition strategies shared by *Rc*Sxph and Na_Vs (17–22). The second triad largely interacts with the C13 carbamate group of STX and is the site of interactions that can enhance STX binding affinity and the ability of *Rc*Sxph to act as a "toxin sponge" that can reverse the effects of STX inhibition of Na_Vs (8, 9).

Although Sxph-like STX binding activity has been reported in extracts from diverse organisms including arthropods (13), amphibians (11, 13, 23), fish (13), and reptiles (13), the molecular origins of this activity have remained obscure. Definition of the *Rc*Sxph STX recognition code enabled identification of 10 new Sxphs from diverse frogs and toads. This substantial enlargement of the Sxph family beyond *Rc*Sxph and the previously identified High Himalaya frog (*Nanorana parkeri*) Sxph (*Np*Sxph) (10) reveals a varied STX binding pocket that surrounds a conserved core of "hot spot"

This article is a PNAS Direct Submission.

[1]Z.C. and S.Z. contributed equally to this work.

[2]To whom correspondence may be addressed. Email: daniel.minor@ucsf.edu.

This article contains supporting information online at http://www.pnas.org/lookup/suppl/doi:10.1073/pnas.2210114119/-/DCSupplemental.

Published October 24, 2022.

positions. Comparison of the new Sxph family members further identifies dramatic differences in the number of thyroglobulin (Thy1) domains inserted into the modified transferrin fold upon which the Sxph family is built. Biochemical characterization of *Np*Sxph, *Oophaga sylvatica* Sxph (*Os*Sxph) (24), *Mantella aurantiaca* Sxph (*Ma*Sxph), and *Ranitomeya imitator* Sxph (*Ri*Sxph), together with structural determination of *Np*Sxph, alone and as STX complexes, shows that the different Sxphs share the capacity to form high-affinity STX complexes and that binding site preorganization (10) is a critical factor for tight STX association. Together, these studies establish an STX molecular recognition code that provides a template for understanding how diverse STX binding proteins engage the toxin and its congeners and uncover that Sxph family members are abundantly found in the most varied and widespread group of amphibians, the anurans. This knowledge and suite of diverse Sxphs, conserved among anuran families separated by at least 140 My of evolution (25), provide a starting point for defining the physiological roles of Sxph in toxin resistance (9, 24, 26), should facilitate identification or design of other STX binding proteins, and may enable the development of new biologics to detect or neutralize STX and related PSPs.

Results

Establishment of a Suite of Assays to Probe *Rc*Sxph Toxin-Binding Properties. To investigate the molecular details of the high-affinity *Rc*Sxph:STX interaction, we developed three assays to assess the effects of STX binding site mutations. A key criterion was to create assays that could be performed in parallel on many *Rc*Sxph mutants using minimal amounts of purified protein and toxin. To this end, we first tested whether we could detect STX binding using a TF assay (27, 28) in which STX binding would manifest as concentration-dependent change in the apparent *Rc*Sxph melting temperature (Tm). Addition of STX, but not the related guanidinium toxin tetrodotoxin (TTX), over a 0-to-20 μM range to samples containing 1.1 μM *Rc*Sxph caused concentration-dependent shifts in the *Rc*Sxph melting curve (Fig. 1*A*) (ΔTm = 3.6 °C ± 0.2 versus 0.3 °C ± 0.4 for STX and TTX, respectively). These differential effects of STX and TTX are in line with the ability of *Rc*Sxph to bind STX (8, 13, 14) but not TTX (8, 9) and indicate that ΔTm is a consequence of the *Rc*Sxph:STX interaction.

To investigate the contributions of residues that comprise the STX binding site, we coupled the TF assay with alanine scanning (15), as well as deeper mutagenesis studies, targeting the eight residues that directly contact STX (Glu540, Phe561, Thr563, Tyr558, Pro727, Phe784, Asp785, and Asp794) (10) and four second-shell sites that support these residues (Tyr795, Ile782, Gln787, and Lys789) (Figs. 1 *A* and *B* and *SI Appendix*, Fig. S1*A*). Measurement of the STX-induced ΔTm changes for the purified *Rc*Sxph mutants revealed ΔTm changes spread over a ∼4 °C range that included ΔTm increases relative to wild type (e.g., I782A and D785N) as well as those that caused complete loss of the thermal shift (e.g., E540A and D794A). All mutations had minimal effects on protein stability (*SI Appendix*, Fig. S1*B*) and there was no evident correlation between Tm and ΔTm (*SI Appendix*, Fig. S1*C*). Hence, the varied ΔTms indicate that each of the 12 positions contributes differently to STX binding.

Because ΔTm interpretation can be complex, especially in the case of a multidomain protein such as *Rc*Sxph, and may not necessarily indicate changes in ligand affinity (27, 28), we developed a second assay to measure the effects of mutations on *Rc*Sxph binding affinity. We synthesized a fluorescein-labeled STX derivative (F-STX) by functionalization of the pendant carbamate group with a six-carbon linker and fluorescein (29, 30) (Fig. 1*C* and *SI Appendix*, Fig. S2) and established an FP assay (31, 32) to measure toxin binding. FP measurements revealed a high-affinity interaction between F-STX and *Rc*Sxph (dissociation constant [K_d] = 7.4 nM ± 2.6) that closely agrees with prior radioligand assay measurements of *Rc*Sxph affinity for STX (∼1 nM) (14). The similarity between the F-STX and STX K_d values is consistent with the expectation from the *Rc*Sxph:STX structure that STX carbamate derivatization should have a minimal effect on binding, as this element resides on the solvent-exposed side of the STX binding pocket (10). To investigate the F-STX interaction further, we soaked *Rc*Sxph crystals with F-STX and determined the structure of the *Rc*Sxph:F-STX complex at 2.65-Å resolution by X-ray crystallography (*SI Appendix*, Fig. S3*A* and Table S1). Inspection of the STX binding pocket revealed clear electron density for the F-STX bis-guanidinium core as well as weaker density that we could assign to the fluorescein heterocycle (*SI Appendix*, Fig. S3*A*), although the high B-factors of the linker and fluorescein indicate that these moieties are highly mobile (*SI Appendix*, Fig. S3*B*). Structural comparison with the *Rc*Sxph:STX complex (10) showed no changes in the core STX binding pose or STX binding pocket residues ($RMSD_{C\alpha}$ = 0.279 Å) (*SI Appendix*, Fig. S3*C*). Together, these data demonstrate that both F-STX and STX bind to Sxph in the same manner and indicate that there are no substantial interactions with the fluorescein label.

FP measurement of the *Rc*Sxph alanine scan mutants uncovered binding affinity changes spanning a ∼13,000-fold range that correspond to free energy perturbations (ΔΔG) of up to ∼5.60 kcal·mol^{-1} (Fig. 1*D*, *SI Appendix*, Fig. S4, and Table 1). The effects were diverse, encompassing enhanced affinity changes (Y558A K_d = 1.2 nM ± 0.3) and large disruptions (E540A K_d = 15.3 μM ± 4.1). As indicated by the TF data, each STX binding pocket residue contributes differently to STX recognition energetics. Comparison of the TF ΔTm and FP ΔΔG values shows a strong correlation between the two measurements (Fig. 1*E*). This concordance between ΔTm and ΔΔG indicates that the changes in unfolding free energies caused by protein mutation and changes in STX binding affinity do not incur large heat capacity or entropy changes relative to the wild-type protein (33, 34). Hence, ΔTm values provide an accurate estimate of the STX binding affinity differences.

To investigate the STX affinity changes further, we used ITC (Fig. 1*F* and *SI Appendix*, Table S2), a label-free method that reports directly on ligand association energetics (35), to examine the interaction of STX with *Rc*Sxph and six mutants having varied effects on binding (E540D, Y558I, Y558A, F561A, P727A, and D794E) (Figs. 1*F* and 2*A* and *SI Appendix*, Fig. S5 *A–C* and Table S2). Experiments with *Rc*Sxph confirm the 1:1 stoichiometry and high affinity of the *Rc*Sxph:STX interaction (K_d ∼nanomolar) reported previously (8, 10, 14) and reveal a large, favorable binding enthalpy (ΔH −16.1 ± 0.2 kcal·mol^{-1}) in line with previous radioligand binding studies (14). In almost all mutants, binding affinity loss correlated with a reduction in enthalpy, consistent with a loss of interactions (*SI Appendix*, Table S2). The one exception to this trend is E540D for which STX association yielded a binding enthalpy (ΔH = −16.3 ± 1.7 kcal·mol^{-1}) very similar to wild-type *Rc*Sxph that was offset by an approximately twofold unfavorable change in binding entropy. The ITC measurements were unable to measure the affinity enhancement for Y558A and Y558I accurately due to the fact that these mutants, as well as *Rc*Sxph, have K_ds at the detection limit of direct titration methods (∼1 nM) (35). Nevertheless,

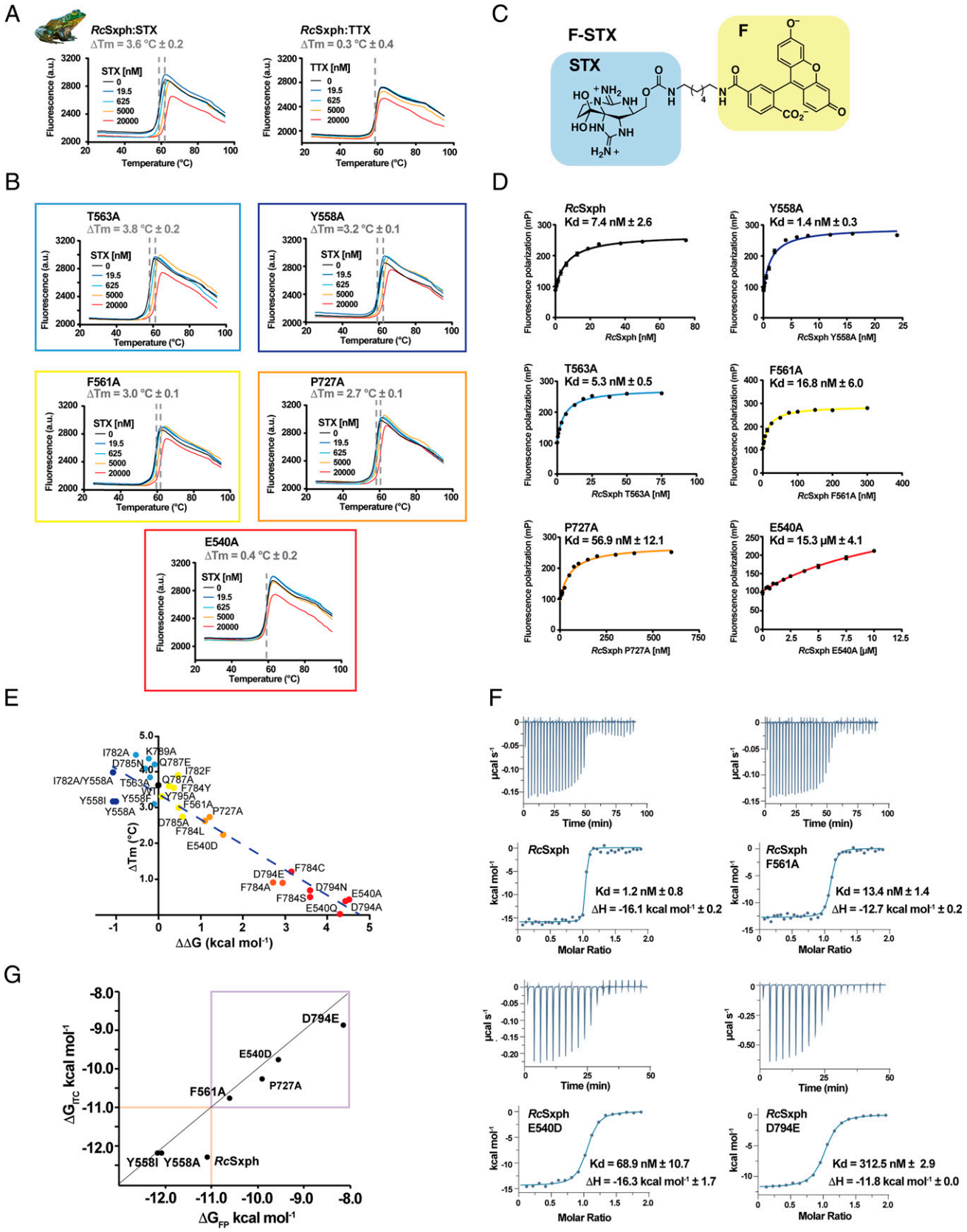

Fig. 1. Alanine scan of *Rc*Sxph binding. (*A* and *B*) Exemplar TF assay results for (*A*) *Rc*Sxph in the presence of the indicated concentrations of STX (*Left*) and TTX (*Right*) and (*B*) select *Rc*Sxph mutants in the presence of STX. STX and TTX concentrations are 0 nM (black), 19.5 nM (blue), 625 nM (cyan), 5,000 nM (orange), and 20,000 nM (red). Gray dashed lines indicate ΔTm. (*C*) F-STX diagram. STX and fluorescein (F) moieties are highlighted in blue and yellow, respectively. (*D*) Exemplar FP binding curves and K_ds for *Rc*Sxph and the indicated mutants. (*E*) Comparison of *Rc*Sxph mutant ΔTm and ΔΔG values (line y = 3.49 –0.7523x, R^2 = 0.886). (*F*) Exemplar isotherms for titration of 100 µM STX into 10 µM *Rc*Sxph. 100 µM STX into 10 µM *Rc*Sxph F561A, 100 µM STX into 10 µM *Rc*Sxph E540D, and 300 µM STX into 30 µM *Rc*Sxph D794E. K_d and ΔH values are indicated. (*G*) Comparison of ΔG_{ITC} for STX and ΔG_{FP} for F-STX for *Rc*Sxph and mutants. Purple box highlights region of good correlation. Orange box indicates region outside of the ITC dynamic range. (line shows x = y). Colors in *B*, *D*, and *E* correspond to classifications in Table 1.

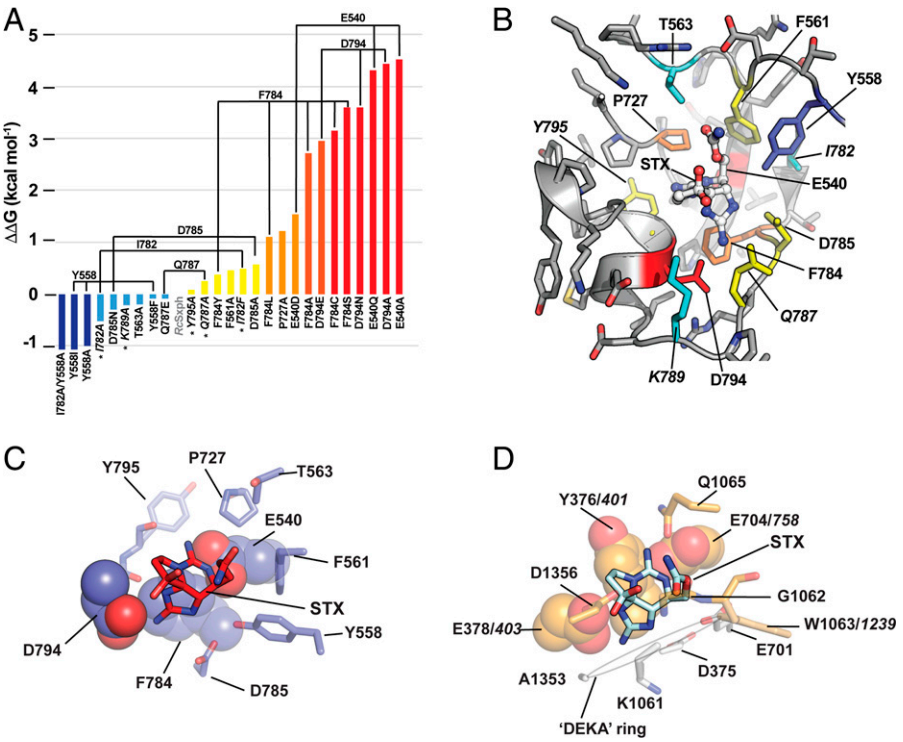

Fig. 2. Energetic fingerprint of STX recognition by *Rc*Sxph. (*A*) ΔΔG comparisons for the indicated *Rc*Sxph STX binding pocket mutants relative to wild-type *Rc*Sxph. Colors indicate ΔΔG < −1 kcal·mol^{-1} (blue), −1 ≤ ΔΔG ≤ 0 kcal·mol^{-1} (light blue), 0 ≥ ΔΔG ≥ 1 kcal·mol^{-1} (yellow), 1 ≥ ΔΔG ≥ 2 kcal·mol^{-1} (orange), 2 ≥ ΔΔG ≥ 3 kcal·mol^{-1} (red orange), and ΔΔG ≥ 3 (red). (*B*) Energetic map of alanine scan mutations on STX binding to the *Rc*Sxph STX binding pocket (PDB ID:6O0F) (10). Second-shell sites are in italics. Colors are as in *A*. (*C* and *D*) Structural interactions of STX with (*C*) *Rc*Sxph (PDB ID:6O0F) (10) and (*D*) human $Na_V1.7$ (PDB ID:6J8G) (40). Residues that are energetically important for the STX interaction are shown in space filling. $Na_V1.7$ selectivity filter "DEKA" ring residues are shown (white). Italics indicate corresponding residue numbers for rat $Na_V1.4$ (18).

ΔG_{ITC} from mutants having STX K_ds within the ITC dynamic range (K_ds ∼30 to 300 nM) showed an excellent agreement with ΔG_{FP} measurements made with F-STX (Fig. 1*G*). These data further validate the TF and FP assay trends and support the conclusion that *Rc*Spxh:F-STX binding interactions are very similar to the *Rc*Spxh:STX interactions. Together, these three assays (Fig. 1 *E* and *G*) provide a robust and versatile suite of options for characterizing STX:Sxph interactions.

Sxph STX binding code is focused on two sets of "hot spot" residues. To understand the structural code underlying STX binding, we classified the effects of the alanine mutations into six groups based on ΔΔG values (Fig. 2*A* and Table 1) and mapped these onto the *Rc*Sxph structure (Fig. 2*B*). This analysis identified a binding "hot spot" comprising three residues that directly contact the STX bis-guanidinium core (Glu540, Phe784, and Asp794) (10) and an additional site near the carbamate (Pro727) where alanine mutations caused substantial STX binding losses (ΔΔG ≥1 kcal·mol^{-1}). Conversely, we also identified a site (Tyr558) where alanine caused a notable enhancement of STX binding (ΔΔG ≤−1 kcal·mol^{-1}) (Fig. 2*B* and Table 1).

To examine the physicochemical nature of key residues critical for STX binding further, we made mutations at select positions guided by the alanine scan. Mutations at Glu540 and Asp794 (10), residues involved in charge pair interactions with the STX guanidinium rings, that neutralized the side chain while preserving shape and volume (Fig. 2*A* and Table 1) disrupted binding strongly, similar to their alanine counterparts (ΔΔG = 4.30 and 3.60 kcal·mol^{-1} for E540Q and D794N, respectively) (Fig. 2*A*, *SI Appendix*, Fig. S4, and Table 1). Altering side-chain length while preserving the negative charge at these sites also greatly diminished STX affinity but was notably less problematic at Glu540 (ΔΔG = 1.54 and 2.94 kcal·mol^{-1} for E540D and D794E, respectively). To probe contacts with Phe784, which makes a cation–π interaction (17) with the STX five-membered guanidinium ring (10), we tested changes that preserved this interface (F784Y), maintained side-chain volume and hydrophobicity (F784L), and that mimicked substitutions (F784C and F784S) found in the analogous residue in STX-resistant Na_Vs ($Na_V1.5$, $Na_V1.8$, and $Na_V1.9$) (10, 17, 19–22) (Fig. 2*A* and Table 1). Preserving the cation–π interaction with F784Y caused a modest binding reduction (ΔΔG = 0.37 kcal·mol^{-1}), whereas F784L was disruptive (ΔΔG = 1.11 kcal·mol^{-1}) and F784C and F784S were even more destabilizing than F784A (ΔΔG = 3.15, 3.60, and 2.71 kcal·mol^{-1}, respectively).

We also examined two other positions that form part of the Sxph binding pocket near the five-membered STX guanidinium ring. Asp785 undergoes the most dramatic conformational change of any residue associated with STX binding, moving from an external-facing conformation to one that engages this STX element (10). Surprisingly, D785A and D785N mutations caused only relatively modest binding changes (Fig. 2*A* and Table 1) (ΔΔG = 0.57 and −0.30 kcal·mol^{-1} for D785A and D785N, respectively). Because of the proximity of the second-shell residue Gln787 to Asp785 and Asp794 (Fig. 2*B*), two residues that coordinate the five-membered STX guanidinium ring (10), we also asked whether adding additional negative charge to this part of the STX binding pocket would enhance toxin binding affinity. However, Q787E had essentially no effect on binding (ΔΔG = −0.09 kcal·mol^{-1}).

Two residues, Tyr558 and Ile782, stood out as sites where alanine substitutions enhanced STX affinity (Fig. 2 *A* and *B* and Table 1). Tyr558 interacts with both the STX five-membered guanidinium ring and carbamate and moves away from the STX binding pocket upon toxin binding (10), whereas Ile782 is a

Table 1. *Rc*Sxph STX binding pocket mutant binding parameters

Class	Construct	K_d, nM	ΔΔG, kcal·mol^{-1}	*n*
Enhanced binding	I782A/Y558A	1.2 ± 0.2	−1.07	6
ΔΔG < −1 kcal·mol^{-1}	Y558I	1.2 ± 0.2	−1.07	6
	Y558A	1.4 ± 0.3	−1.00	6
Mild enhancement	I782A	3.0 ± 0.8	−0.53	4
−1 ≤ ΔΔG ≤ 0 kcal·mol^{-1}	D785N	4.4 ± 0.6	−0.30	4
	K789A	5.1 ± 1.7	−0.22	4
	T563A	5.3 ± 0.5	−0.20	6
	Y558F	6.3 ± 2.3	−0.10	4
	Q787E	6.4 ± 1.6	−0.09	4
	*Rc*Sxph	7.4 ± 2.6	0	10
Mild disruption	Y795A	8.4 ± 2.1	0.08	4
0 ≥ ΔΔG ≥ 1 kcal·mol^{-1}	Q787A	11.3 ± 1.1	0.25	4
	F784Y	13.8 ± 1.0	0.37	4
	I782F	16.1 ± 4.1	0.46	4
	F561A	16.8 ± 6.0	0.48	4
	D785A	19.5 ± 2.5	0.57	4
Disruption	F784L	48.0 ± 6.8	1.11	4
1 ≥ ΔΔG ≥ 2 kcal·mol^{-1}	P727A	56.9 ± 12.1	1.21	4
	E540D	99.9 ± 25.1	1.54	4
Strong disruption	F784A	725.1 ± 108.7	2.71	4
2 ≥ ΔΔG ≥ 3 kcal·mol^{-1}	D794E	1,074.1 ± 69.3	2.94	4
Very strong disruption	F784C	1,510.5 ± 346.1	3.15	4
ΔΔG ≥ 3	D794N	3,228 ± 397	3.60	4
	F784S	3,240 ± 508	3.60	4
	E540Q	10,640 ± 1,325	4.30	4
	D794A	13,172 ± 6,871	4.43	4
	E540A	15,294 ± 4,134	4.52	10

n, number of observations. ΔΔG = RT ln ($K_{dSxph\ mutant}/K_{dSxph}$); T = 298 K. Errors for measurements are SD.

second-shell site that buttresses Tyr558. Hence, we hypothesized that affinity enhancements observed in the Tyr558 and Ile782 mutants resulted from the reduction of Tyr558–STX clashes. In accord with this idea, Y558F had little effect on STX binding (ΔΔG = −0.10 kcal·mol^{-1}), whereas shortening the side chain but preserving its hydrophobic character, Y558I, enhanced binding as much as Y558A (ΔΔG = −1.07 and −1.00 kcal·mol^{-1}, respectively). Conversely, increasing the side-chain volume at the buttressing position, I782F, a change expected to make it more difficult for Tyr558 to move out of the binding pocket, reduced STX binding affinity (ΔΔG = 0.46 kcal·mol^{-1}). Combining the two affinity enhancing mutants, Y558A/I782A, yielded only a marginal increase in affinity in comparison to Y558A (ΔΔG = −1.07 and −1.00 kcal·mol^{-1}, respectively) but was better than I782A alone (ΔΔG = −0.53 kcal·mol^{-1}). This nonadditivity in binding energetics (36) is in line with the physical interaction of the two sites and the direct contacts of Tyr558 with the toxin. Together, these data support the idea that the Tyr558 clash with STX is a key factor affecting STX affinity and suggest that it should be possible to engineer Sxph variants with enhanced binding properties by altering this site.

Taken together, these studies of the energetic map of the *Rc*Sxph STX binding pocket highlight the importance of two amino acid triads. One (Glu540, Phe784, and Asp794) engages the STX bis-guanidinium core of the toxin. The second (Tyr558, Phe561, and Pro727) forms the surface surrounding the carbamate unit (Fig. 2*B*). The central role of the Glu540/Phe784/Asp794 triad in the energetics of binding the bis-guanidinium STX core underscores the toxin receptor site similarities between *Rc*Sxph and Na_Vs (10) (Fig. 2 *C* and *D*). In both, STX binding relies on two acidic residues that coordinate the five- and six-membered STX rings [Sxph Asp794 and Glu540 and rat $Na_V1.4$ Glu403 and Glu758 (18)] and a cation–π interaction [Sxph Phe784 and rat $Na_V1.4$ Tyr401 (18) and its equivalents in other Na_Vs (19–22)]. Hence, both the basic architecture and binding energetics appear to be conserved even though the overall protein structures presenting these elements are dramatically different.

Structures of enhanced-affinity RcSxph mutants. To investigate the structural underpinnings of the affinity enhancement caused by mutations at the Tyr558 site, we determined crystal structures of *Rc*Sxph-Y558A and *Rc*Sxph-Y558I alone (2.60-Å and 2.70-Å resolution, respectively) and as cocrystallized STX complexes (2.60 Å and 2.15 Å, respectively) (*SI Appendix*, Fig. S6 *A–D* and Table S1). Comparison of the apo- and STX-bound structures reveals little movement in the STX binding pocket upon ligand binding ($RMSD_{C\alpha}$ = 0.209 Å and 0.308 Å comparing apo- and STX-bound *Rc*Sxph-Y558A and *Rc*Sxph-Y558I, respectively) (Fig. 3 *A* and *B* and Movies S1 and S2). In both, the largest conformational change is the rotation of Asp785 into the binding pocket to interact with the five-membered guanidinium ring of STX, as seen for *Rc*Sxph (Fig. 3*C*) (10). By contrast, unlike in *Rc*Sxph, there is minimal movement of residue 558 and its supporting loop, indicating that both Y558A and Y558I eliminate the clash incurred by the Tyr558 side chain. Comparison with the *Rc*Sxph:STX complex also shows that the STX carbamate in both structures has moved into a pocket formed by the mutation at Tyr558 ($RMSD_{C\alpha}$ = 0.279 Å and 0.327 Å comparing *Rc*Sxph:STX with *Rc*Sxph-Y558A:STX and *Rc*Sxph-Y558I:STX, respectively) (Fig. 3*C*). This structural change involves a repositioning of the carbamate carbon by 2 Å in the *Rc*Sxph-Y558I:STX complex relative to the *Rc*Sxph:STX complex. These findings are in line with the nearly equivalent toxin-binding affinities of Y558A and Y558I, as well as with the

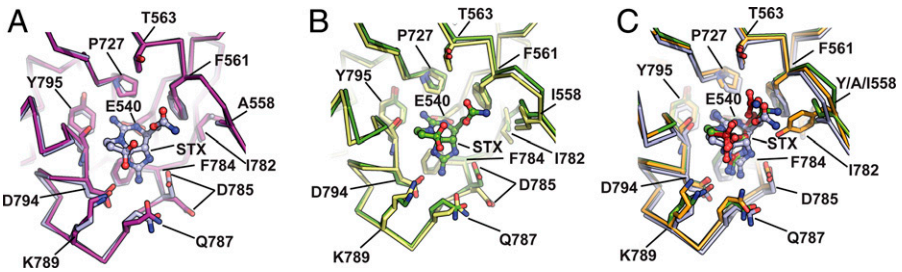

Fig. 3. Structures of enhanced-affinity *Rc*Sxph mutants. (*A*) Superposition of the STX binding pockets of *Rc*Sxph-Y558A (purple) and the *Rc*Sxph-Y558A:STX complex (light blue). (*B*) Superposition of the STX binding pockets of *Rc*Sxph-Y558I (pale yellow) and the *Rc*Sxph-Y558I:STX complex (split pea). (*C*) Superposition of the STX binding pockets of STX bound complexes of *Rc*Sxph (PDB ID: 6O0F) (10), *Rc*Sxph-Y558A (purple), and *Rc*Sxph-Y558I (split pea). STX from the *Rc*Sxph is firebrick.

idea that changes at the Tyr558 buttressing residue, Ile782, relieve the steric clash with STX. They also demonstrate that one strategy for increasing STX affinity is to engineer a highly organized binding pocket that requires minimal conformational changes to bind STX.

Sxph STX binding-affinity changes alter Na_V rescue from STX block. *Rc*Sxph acts as a "toxin sponge" that can reverse STX inhibition of Na_Vs (9). To test the extent to which this property is linked to the intrinsic affinity of *Rc*Sxph for STX, we evaluated how STX-affinity-altering mutations affected *Rc*Sxph rescue of channels blocked by STX. As shown previously, titration of different *Rc*Sxph:STX ratios against *Phyllobates terribilis* $Na_V1.4$ (*Pt*$Na_V1.4$), a Na_V having a concentration that inhibits response by 50% for STX (IC_{50}) of 12.6 nM (9), completely reverses the effects of STX at ratios of 2:1 *Rc*Sxph:STX or greater (Fig. 4 *A* and *F*). Incorporation of mutations that affect STX affinity altered the ability of *Rc*Sxph to rescue Na_Vs and followed the binding assay trends. Mutants that increased STX affinity, Y558I and I782A, improved the ability of *Rc*Sxph to rescue *Pt*$Na_V1.4$ (Effective Rescue Ratio$_{50}$ [ERR_{50}] = 0.81 ± 0.01, 0.87 ± 0.02, and 1.07 ± 0.02 for Y558I, I782A, and *Rc*Sxph, respectively), whereas mutations that compromised STX binding reduced (P727A, ERR_{50} >4) or eliminated (E540A) the ability of *Rc*Sxph to reverse the STX inhibition (Fig. 4 *B*–*F*). This strong correlation indicates that the "toxin sponge" property of Sxph (9) depends on the capacity of Sxph to sequester STX and adds further support to the idea that Sxph has a role in toxin resistance mechanisms (8, 9).

Expansion of the Sxph family. STX binding activity has been reported in the plasma, hemolymph, and tissues of diverse arthropods, amphibians, fish, and reptiles (11, 13), suggesting that many organisms harbor Sxph-like proteins. Besides *Rc*Spxh, similar Sxphs have been identified in only two other frogs, the High Himalaya frog *N. parkeri* (10) and the little devil poison frog *O. sylvatica* (24). As a number of poison frogs exhibit resistance to STX poisoning (9), we asked whether the STX binding site "recognition code" could enable identification of Sxph homologs in other amphibians. To this end, we determined the sequences of 10 new Sxphs (Fig. 5 *A* and *B* and *SI Appendix*, Figs. S7 and S8). These include six Sxphs in two poison dart frog families (family Dendrobatidae: dyeing poison dart frog, *Dendrobates tinctorius*; little devil poison frog, *O. sylvatica*; mimic poison frog, *R. imitator*; golden dart frog, *P. terribilis*; phantasmal poison frog, *Epipedobates tricolor*; and brilliant-thighed poison frog, *Allobates femoralis* and family Mantellidae golden mantella, *M. aurantiaca*) and three Sxphs in toads (Caucasian toad, *Bufo bufo*; Asiatic toad, *Bufo gargarizans*; and South American cane toad, *Rhinella marina*). The identification of the *Os*Sxph sequence confirms its prior identification by mass spectrometry (24) and the discovery of *Rm*Sxph agrees with prior reports of Sxph-like STX binding activity in the cane toad (*R. marina*) (13, 23).

Sequence comparisons (*SI Appendix*, Figs. S7 and S8) show that all of the new Sxphs share the transferrin fold found in *Rc*Sxph comprising N and C lobes each having two subdomains (N1, N2 and C1, C2, respectively) (10, 12) and the signature "EFDD" motif (10) or a close variant in the core of the C-lobe STX binding site (Fig. 5*A*). Similar to *Rc*Sxph, the new Sxphs also have amino acid differences relative to transferrin that should eliminate Fe^{3+} binding (10, 12, 37), as well as a number of protease inhibitor thyroglobulin domains (Thy1) inserted between the N1 and N2 N-lobe subdomains (10, 38) (Fig. 5*A* and *SI Appendix*, Fig. S7–S9). These Thy1 domain insertions range from two in *Rc*Sxph, *Np*Sxph, and *Ma*Sxph to three in the dendrobatid poison frog and cane toad Sxphs to 16 and 15 in toad *Bb*Sxph and *Bg*Sxph, respectively (Fig. 5*A* and *SI Appendix*, Figs. S7–S9).

We used the STX recognition code defined by our studies as a template for investigating cross-species variation in the residues that contribute to STX binding (Fig. 5*B*). This analysis shows a conservation of residues that interact with the STX bis-guanidinium core (Glu540, Phe784, Asp785, Asp794, and Tyr795) and carbamate (Phe561). Surprisingly, five of the Sxphs (*D. tinctorius*, *R. imitator*, *A. femoralis*, *B. bufo,* and *B. gargarizans*) have an aspartate instead of a glutamate at the Glu540 position in *Rc*Sxph that contributes the most binding energy (Fig. 2*A*). The equivalent change in *Rc*Sxph, E540D, reduced STX affinity by ∼100-fold (Table 1) and uniquely alters enthalpy and entropy binding parameters compared to other affinity-lowering mutations (*SI Appendix*, Table S2). Additionally, we identified variations at two sites for which mutations increase *Rc*Sxph STX binding, Tyr558 and Ile782 (Figs. 2*A* and 4 *C* and *E* and Table 1). *Np*Sxph and *Ma*Sxph have an Ile at the Tyr558 site, whereas eight of the new Sxphs have hydrophobic substitutions at the Ile782 position (Fig. 5*B*). The striking conservation of the Sxph scaffold and STX binding site indicate that this class of "toxin sponge" proteins is widespread among diverse anurans, while the amino acid variations in key positions (Glu540, Tyr558, and Ile782) raise the possibility that the different Sxph homologs have varied STX affinity or selectivity for STX congeners.

Diverse Sxph family members have conserved STX binding properties. To explore the STX binding properties of this new set of Sxphs and to begin to understand whether changes in the binding site composition affect toxin affinity, we expressed and purified four representative variants. These included two Sxphs having STX binding-site sequences similar to *Rc*Sxph (*Np*Sxph and *Ma*Sxph) and two Sxphs bearing more diverse amino acid differences (*Ri*Sxph and *Os*Sxph), including one displaying the E540D substitution (*Ri*Sxph). This set also represents Sxphs

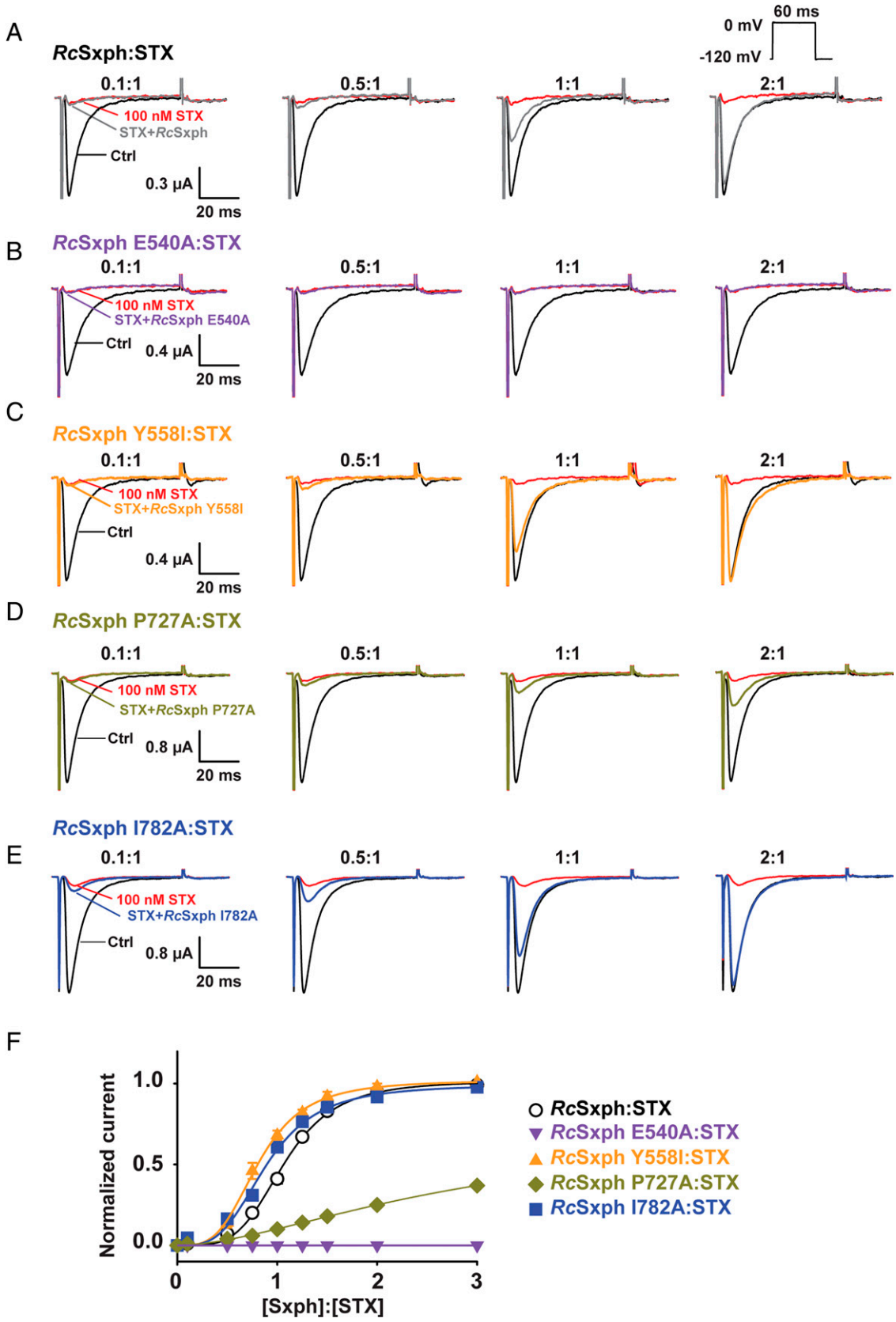

Fig. 4. *Rc*Sxph mutants have differential effects on *Pt*$Na_V1.4$ rescue from STX block. (*A*–*E*) Exemplar two-electrode voltage-clamp recordings of *Pt*$Na_V1.4$ expressed in *Xenopus* oocytes in the presence of 100 nM STX and indicated [Sxph]:[STX] ratios for (*A*) *Rc*Sxph, (*B*) *Rc*Sxph E540A, (*C*) *Rc*Sxph Y558I, (*D*) *Rc*Sxph P727A, and (*E*) *Rc*Sxph I782A. (*Inset*) The stimulation protocol. (*F*) [Sxph]:[STX] dose–response curves for *Rc*Sxph (black open circles), *Rc*Sxph E540A (purple inverted triangles), *Rc*Sxph Y558I (orange triangles), *Rc*Sxph P727A (gold diamonds), and *Rc*Sxph I782A (blue squares) in the presence of 100 nM STX. Lines show fit to the Hill equation.

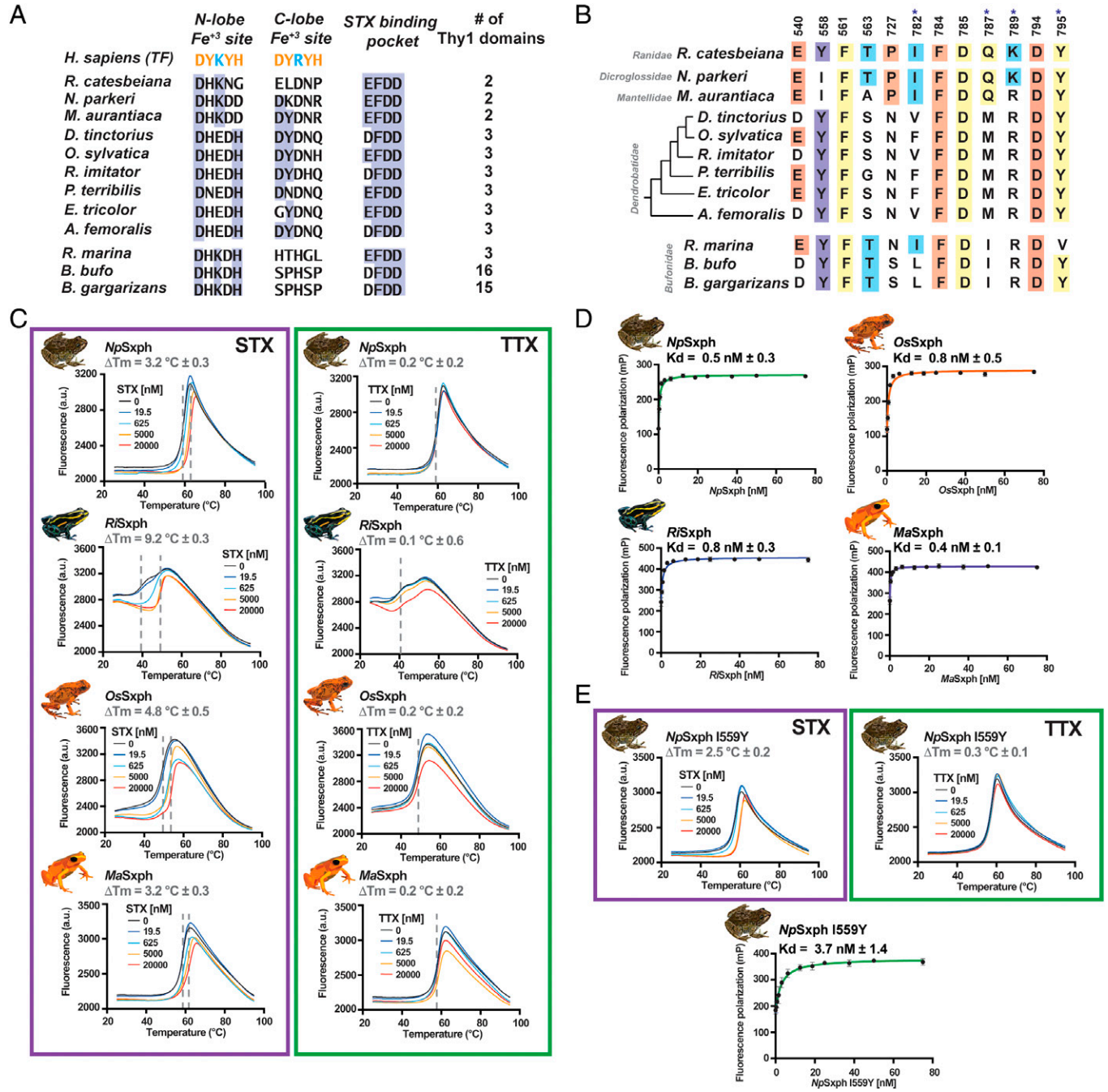

Fig. 5. Sxph family member properties. (*A*) Comparison of the human transferrin (TF) Fe^{3+} ligand positions (UniProtKB: P02787), *Rc*Sxph STX binding motif residues (10), and number of Thy1 domains for Sxphs from *R. castesbeiana* (PDB ID:6O0D) (10), *N. parkeri* (NCBI: XP_018410833.1) (10), *M. aurantiaca*, *D. tinctorius*, *O. sylvatica*, *R. imitator*, *P. terribilis*, *E. tricolor*, *A. femoralis*, *R. marinus*, *B. bufo* (NCBI:XM_040427746.1), and *B. garagarizans* (NCBI:XP_044148290.1). TF Fe^{3+} (orange) and carbonate (blue) ligands are indicated. Blue highlights indicate residue conservation. (*B*) Comparison of STX binding pocket for the indicated Sxphs. Numbers denote *Rc*Sxph positions. Colors indicate the alanine scan classes as in Fig. 3*B*. Conserved residues are highlighted. Asterix indicates second-shell sites. (*C*) Exemplar TF curves for *Np*Sxph, *Ri*Sxph, *Os*Sxph, and *Ma*Sxph in the presence of the indicated concentrations of STX (purple box) or TTX (green box). ΔTm values are indicated. (*D*) Exemplar FP binding curves and K_ds for *Np*Sxph (green), *Ri*Sxph (blue), *Os*Sxph (orange), and *Ma*Sxph (purple). (*E*) Exemplar *Np*Sxph I559Y TF curves in the presence of the indicated concentrations of STX (purple box) or TTX (green box) and FP binding (green). ΔTm and K_d values are indicated. Error bars are SEM.

having either two Thy1 domains similar to *Rc*Sxph (*Np*Sxph and *Ma*Sxph) or three Thy1 domains (*Os*Sxph and *Ri*Sxph) (Fig. 5*A*). TF experiments showed STX-dependent ΔTms for all four Sxphs. By contrast, equivalent concentrations of TTX had no effect (Fig. 5*C*), indicating that, similar to *Rc*Spxh (Fig. 1*A*) (8, 9), all four Sxphs bind STX but not TTX. Unlike the other Sxphs, the *Ri*Sxph melting curve showed two thermal transitions; however, only the first transition was sensitive to STX concentration (Fig. 5*C*). FP binding assays showed that all four Sxphs bound F-STX and revealed affinities stronger than *Rc*Sxph (Fig. 5*D* and Table 2). The enhanced affinity of *Np*Sxph and *Ma*Sxph for STX relative to *Rc*Sxph is consistent with the presence of the Y558I variant (Fig. 5*B*). Importantly, the observation that *Ri*Sxph has a higher affinity for STX than *Rc*Sxph despite the presence of the E540D difference suggests that the other sequence variations in the *Ri*Sxph STX binding pocket compensate for this Glu→Asp change at Glu540.

Table 2. Comparison of Sxph STX binding properties

Construct	K_d, nM	ΔΔG, kcal·mol^{-1}	*n*
*Ma*Sxph	0.4 ± 0.1	−1.73	4
*Np*Sxph	0.5 ± 0.3	−1.60	13
*Ri*Sxph	0.8 ± 0.3	−1.32	4
*Os*Sxph	0.8 ± 0.5	−1.32	10
*Np*Sxph I559Y	3.7 ± 1.4	−0.04	8
*Rc*Sxph	7.4 ± 2.6	0	10

n, number of observations. ΔΔG = RT ln ($K_{d(XSxph)}/K_{d(RcSxph)}$); T = 298 K. Errors for measurements are SD.

Because *Np*Sxph has a higher affinity for STX than *Rc*Sxph (Figs. 1*D* and 5*D* and Table 2) and has an isoleucine at the Tyr558 site (Fig. 5*B*), we asked whether the *Np*Sxph I559Y mutant that converts the *Np*Sxph binding site to match *Rc*Sxph would lower STX affinity. TF measurements showed that *Np*Sxph I559Y had a ∼1 °C smaller ΔTm than *Np*Sxph (ΔTm = 3.2 °C ± 0.3 versus 2.5 °C ± 0.2 for *Np*Sxph and *Np*Sxph I559Y, respectively), indicative of a decreased binding affinity (Fig. 5 *C* and *E*). This result was validated by FP (ΔΔG = −1.56 kcal·mol^{-1}), yielding a result of similar magnitude to the *Rc*Sxph Y558I differences (Fig. 5*E* and Tables 1 and 2). ITC confirmed the high affinity of the interaction (*SI Appendix*, Fig. S5 *D, E* and *F*), but could not yield an explicit K_d given its low nanomolar value (*SI Appendix*, Fig. S5*F*). Nevertheless, these experiments validate the 1:1 stoichiometry of the *Np*Sxph:STX interaction (*SI Appendix*, Table S2) and show that the I559Y change reduced the binding enthalpy, consistent with perturbation of *Np*Sxph:STX interactions (ΔH = −18.7 ± 0.2 vs. −16.8 ± 0.2 kcal·mol^{-1}, *Np*Sxph and *Np*Sxph I559Y, respectively) (*SI Appendix*, Table S2). Taken together, these experiments establish the conserved nature of the STX binding pocket among diverse Sxph homologs and show that the STX recognition code derived from *Rc*Sxph studies (Fig. 5*B*) can identify key changes that influence toxin binding.

Structures of apo- and STX-bound NpSxph reveal a preorganized STX binding site. To compare STX binding modes among Sxph family members, we crystallized and determined the structure of *Np*Sxph, alone and cocrystallized with STX. *Np*Sxph and STX:*Np*Sxph crystals diffracted X-rays to resolutions of 2.2 Å and 2.0 Å, respectively, and were solved by molecular replacement (Fig. 6*A* and *SI Appendix*, Fig. S10 *A* and *B*). As expected from the similarity to *Rc*Sxph, *Np*Sxph is built on a transferrin fold (Fig. 6*A*) and has the same 21 disulfides found in *Rc*Sxph, as well as an additional 22nd disulfide in the Type 1A thyroglobulin domain of *Np*Sxph Thy1-2. However, structural comparison of *Np*Sxph and *Rc*Sxph reveals a number of unexpected large-scale domain rearrangements.

The *Np*Sxph N lobe is displaced along the plane of the molecule by ∼30° and rotated around the central axis by a similar amount (*SI Appendix*, Fig. S10*C*). *Np*Sxph N lobe and C lobe lack Fe^{3+} binding sites (Fig. 5*A*), and despite the N-lobe displacement relative to *Rc*Sxph adopt closed and open conformations, respectively, as in *Rc*Sxph (10) (*SI Appendix*, Fig. S10 *D* and *E*) ($RMSD_{Cα}$ = 1.160 Å and 1.373 Å for *Np*Sxph and *Rc*Sxph N and C lobes, respectively). Surprisingly, the two *Np*Sxph Thy1 domains are in different positions than in *Rc*Sxph and appear to move as a unit by ∼90° with respect to the central transferrin scaffold (*SI Appendix*, Fig. S10*F* and Movie S3) and a translation of ∼30 Å of Thy1-2 (*SI Appendix*, Fig. S10*G*). Thy1-1 is displaced from a site over the N lobe in *Rc*Sxph to one in which it interacts with the *Np*Sxph C-lobe C2 subdomain and Thy1-2 moves from between the N and C lobes in *Rc*Sxph where it interacts with the C1 subdomain, to a position in *Np*Sxph where it interacts with both N-lobe subdomains. Consequently, the interaction between the C-lobe β-strand β7C1 and Thy1-2 β5 observed in *Rc*Sxph is absent in *Np*Sxph. Despite these domain-scale differences, Thy1-1 and Thy1-2 are structurally similar to each other ($RMSD_{Cα}$ = 1.056 Å) and to their *Rc*Sxph counterparts (*SI Appendix*, Fig. S10*H*) ($RMSD_{Cα}$ = 1.107 Å and 0.837, respectively). Further, none of these large-scale changes impact the STX binding site, which is found on the C1 domain as in *Rc*Sxph (Fig. 5*A*).

Comparison of the apo- and STX-bound *Np*Sxph structures shows that there are essentially no STX binding site conformational changes upon STX engagement, apart from the movement of Asp786 to interact with the STX five-membered guanidinium ring (Fig. 6*B* and Movie S4). This conformational change is shared with *Rc*Sxph (10) and appears to be a common element of Sxph binding to STX. The movements of Tyr558 and its loop away from the STX binding site observed in *Rc*Sxph (10) are largely absent in *Np*Sxph for the Tyr558 equivalent position, Ile559, and its supporting loop. Hence, the *Np*Sxph STX binding site is better-organized to accommodate STX (Fig. 6*B*), similar to *Rc*Sxph Y558I (Fig. 3*B*). We also noted an electron density in the apo-*Np*Sxph STX binding site that we assigned as a PEG400 molecule from the crystallization solution (*SI Appendix*, Fig. S10*A*). This density occupies a site different from STX and is not present in the STX-bound complex (*SI Appendix*, Fig. S10*B*). Its presence suggests that other molecules may be able to bind the STX binding pocket. Similar to *Rc*Sxph, the *Np*Sxph STX binding site is very electronegative (*SI Appendix*, Fig. S11), consistent with the strong conservation of the E540 and D794 positions (Fig. 5 *A* and *B*) that are the most energetically important and coordinate the positively charged STX bis-guanidinium core (Fig. 2 *A* and *B* and Table 1).

We also determined the structure of an *Np*Sxph:F-STX complex at 2.2-Å resolution (*SI Appendix*, Table S1). This structure shows no density for the fluorescein moiety and has an identical STX pose to the *Np*Sxph:STX complex (*SI Appendix*, Fig. S12). These data provide further evidence that fluorescein does not interact with Sxph (cf. *SI Appendix*, Fig. S3) even though it is tethered to the STX binding pocket and support the idea that the FP assay faithfully reports on Sxph:STX interactions. Comparison of the *Np*Sxph and *Rc*Spxh STX poses shows essentially identical interactions with the tricyclic bis-guanidinium core and reveals that the carbamate is able to occupy the pocket opened by the Y→I variant (Fig. 6*C*), as observed in *Rc*Sxph Y558I (Fig. 3*B*). This change, together with the more rigid nature of the *Np*Sxph STX binding pocket, likely contributes to the higher affinity of *Np*Sxph for STX relative to *Rc*Sxph (Table 1). Taken together, the various structures of Sxph:STX complexes show how subtle changes, particularly at the Tyr558 position, can influence STX binding and underscore that knowledge of the STX binding code can be used to tune the STX binding properties of different Sxphs.

Discussion

Our biochemical and structural characterization of a set of *Rc*Sxph mutants and Sxphs from diverse anurans reveals a conserved STX recognition code centered around six amino acid residues comprising two triads. One triad engages the STX

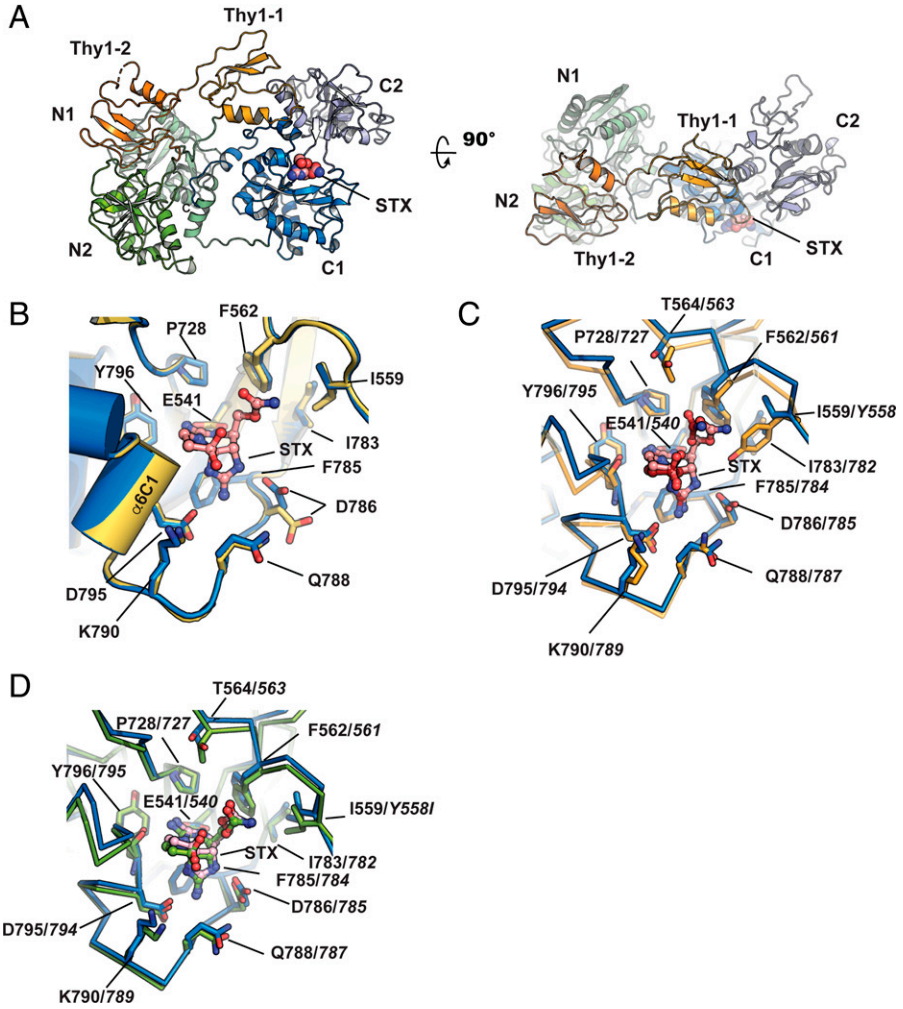

Fig. 6. *Np*Sxph and *Np*Sxph:STX structures. (*A*) Cartoon diagram of the *Np*Sxph:STX complex. N1 (light green), N2 (green), Thy1-1 (light orange), Thy1-2 (orange), C1 (marine), and C2 (light blue) domains are indicated. STX (pink) is shown in space-filling representation. (*B*) Comparison of STX binding pocket for apo-*Np*Sxph (yellow) and *Np*Sxph:STX (marine). STX (pink) is shown as ball and stick. (*C*) Comparison of *Np*Sxph (marine) and *Rc*Sxph (orange) (PDB ID:6O0F) (10) STX binding sites. STX from *Np*Sxph and *Rc*Sxph complexes is pink and orange, respectively. (*D*) Comparison of *Np*Sxph (marine) and *Rc*Sxph-Y558I (split pea) STX binding sites. STX from *Np*Sxph and *Rc*Sxph-Y558I complexes is pink and split pea, respectively. *Rc*Sxph and *Rc*Sxph-Y558I residue numbers in *C* and *D* are indicated in italics.

bis-guanidinium core using carboxylate groups that coordinate each ring (*Rc*Sxph Glu540 and Asp794) and an aromatic residue that makes a cation–π interaction (*Rc*Sxph Phe784) with the STX concave face. This recognition motif is shared with Na_Vs, the primary target of STX in PSP (18, 39, 40) (Fig. 2 *C* and *D*), and showcases a remarkably convergent STX recognition strategy for the tricyclic, bis-guandinium STX core. The second amino acid triad (*Rc*Sxph residues Tyr558, Phe561, and Pro727) largely interacts with the carbamate moiety and contains a site, Tyr558, and its supporting residue, Ile782, where amino acid changes, including those found in some anuran Sxphs (Fig. 5), enhance STX binding. Structural studies of *Rc*Sxph mutants and the High Himalaya frog *Np*Sxph show that STX-affinity-enhancing substitutions in this area of the binding pocket act by reducing the degree of conformational change associated with STX binding (Figs. 3 and 6 *C* and *D*). These findings reveal one strategy for creating high-affinity STX binding sites. Importantly, enhancing the affinity of Sxph for STX through changes at either residue increases the capacity of *Rc*Sxph to rescue Na_Vs from STX block (Fig. 4), demonstrating that an understanding of the STX recognition code enables rational modification of Sxph binding properties. Thus, exploiting the information in the STX recognition code defined here should enable design of Sxphs as STX sensors or agents for treating STX poisoning.

Although STX binding activity has been reported in a variety of diverse invertebrates (13) and vertebrates (13, 23), only two types of STX binding proteins have been identified and validated, frog Sxphs (8, 9) and the pufferfish STX and TTX binding proteins (41, 42). Our discovery of a set of 10 new Sxphs that bind STX with high affinity (Fig. 5 and *SI Appendix*, Figs. S7 and S8) that share a conserved STX binding site represents a substantial expansion of the Sxph family and reveals natural variation in the residues that are important for STX binding (Fig. 5*B*). Most notably, E540D, a change that reduces STX binding in *Rc*Sxph by ∼14-fold, occurs in five of the newly identified Sxphs. Nevertheless, functional studies show that *Rt*Sxph, which bears an Asp at this site, binds STX more strongly than *Rc*Sxph (Table 2). Hence, the natural variations at other STX binding pocket residues must provide compensatory interactions to maintain a high STX binding affinity. Understanding how such variations impact STX engagement or influence the capacity of these proteins to discriminate among STX congeners (13) remain important unanswered questions. The striking abundance of Sxphs in diverse amphibians, representing lineages separated by ∼140 My (25) and that are not known to carry STX, raises intriguing questions

regarding the selective pressures that have caused these disparate amphibians to maintain this STX binding protein and its capacity to sequester this lethal toxin.

Besides the conserved STX binding site, all of the amphibian Sxphs possess a set of Thy1 domains similar to those in *Rc*Sxph that have been shown to act as protease inhibitors (38). Comparison of anuran Sxphs shows that these domains are a common feature of the Sxph family and occur in strikingly varied numbers, comprising two or three in most Sxphs but having a remarkable expansion to 15 to 16 in some toad Sxphs (Fig. 5*A* and *SI Appendix*, Fig. S7–S9). Structural comparisons between *Rc*Sxph and *Np*Sxph, representing the class that has two Thy1 domains (Fig. 5*A*), show that these domains can adopt different positions with respect to the shared, modified transferrin core (*SI Appendix*, Fig. S10*F*). Whether the Sxph Thy1 domains and their varied numbers are important for Sxph-mediated toxin resistance mechanisms (8, 9) or serve some other function remains unknown. Our definition of the Sxph STX binding code, which provides a guide for deciphering variation in the Sxph STX binding site (Fig. 5*B*), and discovery of high variability in Thy1 repeats among anuran Sxphs constitutes a template for identifying other Sxphs within this widespread and diverse family of amphibians.

STX interacts with a variety of target proteins including select Na_V isoforms (43), other channels (44, 45), diverse soluble STX binding proteins (8, 10, 41, 42, 46, 47), and some enzymes (3, 48, 49). The identification of the Sxph STX recognition code together with the substantial expansion of the Sxph family provides a foundation for developing a deeper understanding of the factors that enable proteins to bind STX. Exploration of such factors should be facilitated by the assays established here that allow Sxph:STX interactions to be probed using a range of sample quantities (TF: 25 μg Sxph, 600 ng STX; FP: 3 μg Sxph, 1 ng F-STX; ITC: 300 μg Sxph, 5 μg STX) and that should be adaptable to other types of STX targets. In cases of limited samples, such as difficult to obtain STX congeners, the excellent agreement among the assays should provide a reliable basis for interpretation of Sxph binding properties. Our delineation of the Sxph STX binding code and discovery of numerous Sxph family homologs among diverse amphibians set a broad framework for understanding the lethal effects of this potent neurotoxin and "toxin sponge" STX resistance mechanisms (8, 9). This knowledge may enable the design of novel PSP toxin sensors and agents that could mitigate STX intoxication.

Materials and Methods

R. catesbeiana Sxph (*Rc*Sxph), *N. parkeri* Sxph (*Np*Sxph), *M. aurantiaca* Sxph (*Ma*Sxph), *O. sylvatica* Sxph (*Os*Sxph), and *R. imitator* Sxph (*Ri*Sxph), and mutants were expressed and purified using a previously described *Rc*Sxph baculovirus expression system (10). TF assays for STX and TTX binding were developed as outlined in ref. 27. FP assays were performed as described (50). Structure determination was done following previously described methods for *Rc*Sxph (10). Two-electrode voltage clamp experiments evaluating *Rc*Sxph rescue of Na_Vs from STX block were done as previously described (9). Details on cloning, expression, purification, binding assays, electrophysiology, structure determination, and F-STX synthesis can be found in *SI Appendix*.

Data, Materials, and Software Availability. Sequences of *AfSxph* (OP265195), *DtSxph* (OP265194), *EtSxph* (OP265196), *MaSxph* (OP265197), *OsSxph* (OP311630), *PtSxph* (OP267560), *RiSxph* (OP265193), and *RmSxph* (OP267561) have been deposited and are available from the National Center for Biotechnology Information GenBank. Coordinates and structure factors and for *Rc*Sxph-Y558A (8D6P) (51), *Rc*Sxph-Y558A:STX (8D6S) (52), *Rc*Sxph Y558I (8D6Q) (53), *Rc*Sxph-Y558I:STX (8D6T) (54), *Rc*Sxph:F-STX (8D6U) (55), *Np*Sxph (8D6G) (56), *Np*Sxph:STX (8D6M) (57), and *Np*Sxph:F-STX (8D6O) (58) have been deposited in the RCSB Protein Data Bank.

ACKNOWLEDGMENTS. We thank Z. Wong and T.-J. Yen for technical help and K. Brejc and J. Gross for comments on the manuscript. This work was supported by grants Department of Defense (DoD) HDTRA-1-19-1-0040 and HDTRA-1-21-1-10011 and University of California, San Francisco Program for Breakthrough Biomedical Research, which is partially funded by the Sandler Foundation, to D.L.M., NSF-1822025 to L.A.O, NIH-NIGMS R01-GM117263-05 to J.D.B., an American Heart Association postdoctoral fellowship to F.A.-A, an NSF GRFP (DGE-1656518) and HHMI Gilliam Fellowship (GT13330) to A.A.-B., and a DoD National Defense Science and Engineering Graduate (NDSEG) Fellowship to H.S.H. H.S.H. is a Center for Molecular Analysis and Design Fellow at Stanford University.

Author affiliations: [a]Cardiovascular Research Institute, University of California, San Francisco, CA 94158; [b]Department of Chemistry, Stanford University, Stanford, CA 94305; [c]Department of Biology, Stanford University, Stanford, CA 94305; [d]Department of Biochemistry and Biophysics, University of California, San Francisco, CA 94158; [e]Department of Cellular and Molecular Pharmacology, University of California, San Francisco, CA 94158; [f]California Institute for Quantitative Biomedical Research, University of California, San Francisco, CA 94158; [g]Kavli Institute for Fundamental Neuroscience, University of California, San Francisco, CA 94158; and [h]Molecular Biophysics and Integrated Bioimaging Division, Lawrence Berkeley National Laboratory, Berkeley, CA 94720

Author contributions: Z.C., S.Z., H.S.H., A.A.-B., L.A.O., J.D.B., and D.L.M. designed research; Z.C., S.Z., H.S.H., A.A.-B., F.A.-A., M.B., and D.R. performed research; H.S.H. and J.D.B. contributed new reagents/analytic tools; Z.C., S.Z., A.A.-B., F.A.-A., L.A.O., J.D.B., and D.L.M. analyzed data; and Z.C., S.Z., H.S.H., A.A.-B., L.A.O., J.D.B., and D.L.M. wrote the paper.

Competing interest statement: J.D.B. is a cofounder and holds equity shares in SiteOne Therapeutics, Inc., a start-up company interested in developing subtype-selective modulators of sodium channels. The other authors declare no competing interests.

1. A. P. Thottumkara, W. H. Parsons, J. Du Bois, Saxitoxin. *Angew. Chem. Int. Ed. Engl.* **53**, 5760–5784 (2014).
2. B. Hille, *Ion Channels of Excitable Membranes* (Sinauer Associates, Inc., Sunderland, MA, ed. 3, 2001).
3. L. E. Llewellyn, Saxitoxin, a toxic marine natural product that targets a multitude of receptors. *Nat. Prod. Rep.* **23**, 200–222 (2006).
4. M. Wiese, P. M. D'Agostino, T. K. Mihali, M. C. Moffitt, B. A. Neilan, Neurotoxic alkaloids: Saxitoxin and its analogs. *Mar. Drugs* **8**, 2185–2211 (2010).
5. D. M. Anderson *et al.*, Evidence for massive and recurrent toxic blooms of *Alexandrium catenella* in the Alaskan Arctic. *Proc. Natl. Acad. Sci. U.S.A.* **118**, e2107387118 (2021).
6. M. Prinzmetal, H. Sommer, C. D. Leake, The pharmacological action of "mussel poison". *J. Pharmacol. Exp. Ther.* **46**, 63–73 (1932).
7. C. Y. Kao, F. A. Fuhrman, Differentiation of the actions of tetrodotoxin and saxitoxin. *Toxicon* **5**, 25–34 (1967).
8. J. Mahar, G. L. Lukács, Y. Li, S. Hall, E. Moczydlowski, Pharmacological and biochemical properties of saxiphilin, a soluble saxitoxin-binding protein from the bullfrog (Rana catesbeiana). *Toxicon* **29**, 53–71 (1991).
9. F. Abderemane-Ali *et al.*, Evidence that toxin resistance in poison birds and frogs is not rooted in sodium channel mutations and may rely on "toxin sponge" proteins. *J. Gen. Physiol.* **153**, e202112872 (2021).
10. T.-J. Yen, M. Lolicato, R. Thomas-Tran, J. Du Bois, D. L. Minor Jr., Structure of the saxiphilin:saxitoxin (STX) complex reveals a convergent molecular recognition strategy for paralytic toxins. *Sci. Adv.* **5**, eaax2650 (2019).
11. D. D. Doyle, M. Wong, J. Tanaka, L. Barr, Saxitoxin binding sites in frog-myocardial cytosol. *Science* **215**, 1117–1119 (1982).
12. M. A. Morabito, E. Moczydlowski, Molecular cloning of bullfrog saxiphilin: A unique relative of the transferrin family that binds saxitoxin. *Proc. Natl. Acad. Sci. U.S.A.* **91**, 2478–2482 (1994).
13. L. E. Llewellyn, P. M. Bell, E. G. Moczydlowski, Phylogenetic survey of soluble saxitoxin-binding activity in pursuit of the function and molecular evolution of saxiphilin, a relative of transferrin. *Proc. Biol. Sci.* **264**, 891–902 (1997).
14. L. E. Llewellyn, E. G. Moczydlowski, Characterization of saxitoxin binding to saxiphilin, a relative of the transferrin family that displays pH-dependent ligand binding. *Biochemistry* **33**, 12312–12322 (1994).
15. T. Clackson, J. A. Wells, A hot spot of binding energy in a hormone-receptor interface. *Science* **267**, 383–386 (1995).
16. J. A. Wells, Systematic mutational analyses of protein-protein interfaces. *Methods Enzymol.* **202**, 390–411 (1991).
17. D. T. Infield *et al.*, Cation-π interactions and their functional roles in membrane proteins. *J. Mol. Biol.* **433**, 167035 (2021).
18. R. Thomas-Tran, J. Du Bois, Mutant cycle analysis with modified saxitoxins reveals specific interactions critical to attaining high-affinity inhibition of hNaV1.7. *Proc. Natl. Acad. Sci. U.S.A.* **113**, 5856–5861 (2016).
19. S. H. Heinemann, H. Terlau, K. Imoto, Molecular basis for pharmacological differences between brain and cardiac sodium channels. *Pflugers Arch.* **422**, 90–92 (1992).
20. J. Satin *et al.*, A mutant of TTX-resistant cardiac sodium channels with TTX-sensitive properties. *Science* **256**, 1202–1205 (1992).

21. A. Leffler, R. I. Herzog, S. D. Dib-Hajj, S. G. Waxman, T. R. Cummins, Pharmacological properties of neuronal TTX-resistant sodium channels and the role of a critical serine pore residue. *Pflugers Arch.* **451**, 454–463 (2005).
22. L. Sivilotti, K. Okuse, A. N. Akopian, S. Moss, J. N. Wood, A single serine residue confers tetrodotoxin insensitivity on the rat sensory-neuron-specific sodium channel SNS. *FEBS Lett.* **409**, 49–52 (1997).
23. J. C. Tanaka, D. D. Doyle, L. Barr, Sodium channels in vertebrate hearts. Three types of saxitoxin binding sites in heart. *Biochim. Biophys. Acta* **775**, 203–214 (1984).
24. S. N. Caty *et al.*, Molecular physiology of chemical defenses in a poison frog. *J. Exp. Biol.* **222**, jeb204149 (2019).
25. Y. J. Feng *et al.*, Phylogenomics reveals rapid, simultaneous diversification of three major clades of Gondwanan frogs at the Cretaceous-Paleogene boundary. *Proc. Natl. Acad. Sci. U.S.A.* **114**, E5864–E5870 (2017).
26. L. A. O'Connell *et al.*; LS50: Integrated Science Laboratory Course, Rapid toxin sequestration modifies poison frog physiology. *J. Exp. Biol.* **224**, jeb230342 (2021).
27. K. Huynh, C. L. Partch, Analysis of protein stability and ligand interactions by thermal shift assay. *Curr. Protoc. Protein Sci.* **79**, 28.9.1–28.9.14 (2015).
28. F. H. Niesen, H. Berglund, M. Vedadi, The use of differential scanning fluorimetry to detect ligand interactions that promote protein stability. *Nat. Protoc.* **2**, 2212–2221 (2007).
29. B. M. Andresen, J. Du Bois, De novo synthesis of modified saxitoxins for sodium ion channel study. *J. Am. Chem. Soc.* **131**, 12524–12525 (2009).
30. A. E. Ondrus *et al.*, Fluorescent saxitoxins for live cell imaging of single voltage-gated sodium ion channels beyond the optical diffraction limit. *Chem. Biol.* **19**, 902–912 (2012).
31. X. Huang, A. Aulabaugh, Application of fluorescence polarization in HTS assays. *Methods Mol. Biol.* **1439**, 115–130 (2016).
32. H. Zhang, Q. Wu, M. Y. Berezin, Fluorescence anisotropy (polarization): From drug screening to precision medicine. *Expert Opin. Drug Discov.* **10**, 1145–1161 (2015).
33. W. J. Becktel, J. A. Schellman, Protein stability curves. *Biopolymers* **26**, 1859–1877 (1987).
34. C. Arrigoni, D. L. Minor, Jr, Global versus local mechanisms of temperature sensing in ion channels. *Pflugers Arch.* **470**, 733–744 (2018).
35. A. Velazquez-Campoy, H. Ohtaka, A. Nezami, S. Muzammil, E. Freire, Isothermal titration calorimetry. *Curr. Protoc. Cell. Biol.* **Chapter 17**, Unit 17 18 (2004).
36. J. A. Wells, Additivity of mutational effects in proteins. *Biochemistry* **29**, 8509–8517 (1990).
37. Y. Li, L. Llewellyn, E. Moczydlowski, Biochemical and immunochemical comparison of saxiphilin and transferrin, two structurally related plasma proteins from Rana catesbeiana. *Mol. Pharmacol.* **44**, 742–748 (1993).
38. B. Lenarčič *et al.*, Saxiphilin, a saxitoxin-binding protein with two thyroglobulin type 1 domains, is an inhibitor of papain-like cysteine proteinases. *J. Biol. Chem.* **275**, 15572–15577 (2000).
39. H. Shen *et al.*, Structural basis for the modulation of voltage-gated sodium channels by animal toxins. *Science* **362**, eaau2596 (2018).
40. H. Shen, D. Liu, K. Wu, J. Lei, N. Yan, Structures of human $Na_v1.7$ channel in complex with auxiliary subunits and animal toxins. *Science* **363**, 1303–1308 (2019).
41. M. Yotsu-Yamashita *et al.*, Purification, characterization, and cDNA cloning of a novel soluble saxitoxin and tetrodotoxin binding protein from plasma of the puffer fish, Fugu pardalis. *Eur. J. Biochem.* **268**, 5937–5946 (2001).
42. M. Yotsu-Yamashita, H. Yamaki, N. Okoshi, N. Araki, Distribution of homologous proteins to puffer fish saxitoxin and tetrodotoxin binding protein in the plasma of puffer fish and among the tissues of Fugu pardalis examined by Western blot analysis. *Toxicon* **55**, 1119–1124 (2010).
43. L. M. Durán-Riveroll, A. D. Cembella, Guanidinium toxins and their interactions with voltage-gated sodium ion channels. *Mar. Drugs* **15**, 303 (2017).
44. Z. Su, M. Sheets, H. Ishida, F. Li, W. H. Barry, Saxitoxin blocks L-type ICa. *J. Pharmacol. Exp. Ther.* **308**, 324–329 (2004).
45. J. Wang, J. J. Salata, P. B. Bennett, Saxitoxin is a gating modifier of HERG K+ channels. *J. Gen. Physiol.* **121**, 583–598 (2003).
46. N. Takati, D. Mountassif, H. Taleb, K. Lee, M. Blaghen, Purification and partial characterization of paralytic shellfish poison-binding protein from Acanthocardia tuberculatum. *Toxicon* **50**, 311–321 (2007).
47. H. Lin *et al.*, Neutralizing effect of hemolymph from the shore crab, Thalamita crenata, on paralytic shellfish toxins. *Toxicon* **99**, 51–57 (2015).
48. A. L. Lukowski *et al.*, Biocatalytic detoxification of paralytic shellfish toxins. *ACS Chem. Biol.* **14**, 941–948 (2019).
49. A. L. Lukowski, J. Liu, J. Bridwell-Rabb, A. R. H. Narayan, Structural basis for divergent C-H hydroxylation selectivity in two Rieske oxygenases. *Nat. Commun.* **11**, 2991 (2020).
50. A. M. Rossi, C. W. Taylor, Analysis of protein-ligand interactions by fluorescence polarization. *Nat. Protoc.* **6**, 365–387 (2011).
51. Z. Chen *et al.*, Definition of a saxitoxin (STX) binding code enables discovery and characterization of the anuran saxiphilin family. PDB. https://www.rcsb.org/structure/unreleased/8D6P. Deposited 6 June 2022.
52. Z. Chen *et al.*, Definition of a saxitoxin (STX) binding code enables discovery and characterization of the anuran saxiphilin family. PDB. https://www.rcsb.org/structure/unreleased/8D6S. Deposited 6 June 2022.
53. Z. Chen *et al.*, Definition of a saxitoxin (STX) binding code enables discovery and characterization of the anuran saxiphilin family. PDB. https://www.rcsb.org/structure/unreleased/8D6Q. Deposited 6 June 2022.
54. Z. Chen *et al.*, Definition of a saxitoxin (STX) binding code enables discovery and characterization of the anuran saxiphilin family. PDB. https://www.rcsb.org/structure/unreleased/8D6T. Deposited 6 June 2022.
55. Z. Chen *et al.*, Definition of a saxitoxin (STX) binding code enables discovery and characterization of the anuran saxiphilin family. PDB. https://www.rcsb.org/structure/unreleased/8D6U. Deposited 6 June 2022.
56. Z. Chen *et al.*, Definition of a saxitoxin (STX) binding code enables discovery and characterization of the anuran saxiphilin family. PDB. https://www.rcsb.org/structure/unreleased/8D6G. Deposited 6 June 2022.
57. Z. Chen *et al.*, Definition of a saxitoxin (STX) binding code enables discovery and characterization of the anuran saxiphilin family. PDB. https://www.rcsb.org/structure/unreleased/8D6M. Deposited 6 June 2022.
58. Z. Chen *et al.*, Definition of a saxitoxin (STX) binding code enables discovery and characterization of the anuran saxiphilin family. PDB. https://www.rcsb.org/structure/unreleased/8D6O. Deposited 6 June 2022.